Relief history and denudation evolution of the northern Tibet margin: Constraints from ^{40}Ar/^{39}Ar and (U–Th)/He dating and implications for far-field effect of rising plateau

Fei Wang [a,b,*], Huile Feng [a], Wenbei Shi [a], Weibin Zhang [a], Lin Wu [a], Liekun Yang [a], Yinzhi Wang [a], Zhigang Zhang [a], Rixiang Zhu [a]

[a] State Key Laboratory of Lithospheric Evolution, Institute of Geology and Geophysics, Chinese Academy of Sciences, Beijing 100029, PR China
[b] CAS Center for Excellence in Tibetan Plateau Earth Sciences, PR China

ABSTRACT

How does the rising Tibetan Plateau affect its peripheral region? The current understanding of the mechanism of orogenic plateau development is incomplete and thus no consensus yet exists in this regard. However, our new ^{40}Ar/^{39}Ar and (U–Th)/He dataset presented in this study may shed some light on this issue. ^{40}Ar/^{39}Ar dating, on two vertical transects from the massif between Nuomuhong and Golmud, indicates that the Eastern Kunlun Range was built-up and exhumed during the later Triassic initially, and a minimum overburden of ~11.7–14.0 km has been eroded since ~220 Ma. (U–Th)/He age–elevation relationships (AERs) indicate a rapid exhumation event at ~40 Ma following a long period of slow exhumation phase from late Mesozoic to early Eocene time. In this study, two scenarios – one assuming a single stage and the other assuming multiple stages of evolution history – are modeled. Modeling of a multiple stage scenario is reasonable and is able to reflect the "actual" situation, which reveals the entire denudation and relief history of the northern Tibet from late Mesozoic to the present time. After prolonged denudation before 50 Ma, a low topography (~0.17 times the relief of the present) developed by 50 Ma with an erosion rate of $0.013^{+0.025}_{-0.013}$ mm/yr. The highest relief (~1.82 times the relief of the present) of the Cenozoic time came into being at 40 Ma with an erosion rate of 0.052 ± 0.025 mm/yr, which was possibly a result of the collision between India and Eurasia. Subsequently, the relief steadily decreased to the present level due to continued denudation. This suggests that deformation propagation from the continued convergence boundary between India and Eurasia was insignificant after the construction of the highest relief. This observation is broadly consistent with published accounts on the stratigraphic, cooling, and faulting histories of the northern Tibet margin.

1. Introduction

The consequences of the far-field effect of continued Eurasia–Indian convergence since ~50 Ma (Rowley, 1996; Wang et al., 2011) on the northern Tibet margin have been a topic of debate (Tapponnier et al., 2001; Meng and Fang, 2008). This issue is further complicated by a possible linkage between climate change and the uplift of mountain belts. It is believed that alternating glacial and interglacial conditions and increased denudation rates during the Late Cenozoic (Zhang et al., 2001; Molnar, 2004; Valla et al., 2010; van der Beek et al., 2010) can result in isostatic uplift of mountain peaks (Molnar and England, 1990) and thus increase unroofing and cooling of an area (Montgomery, 1994; Small and Anderson, 1998; Champagnac et al., 2007; van der Beek et al., 2010) through perturbation of the underground thermal structure

(Braun, 2003). Erosion occurs mainly in the valleys leading to the high relief mountain belts. Therefore, understanding the evolution of topography requires a better comprehension of the linkage between climate, tectonics, and surface processes (Beaumont et al., 1992; Zeitler et al., 2001; Valla et al., 2010).

The terrain along the northern margin of the Tibetan Plateau has been well-studied for its rising-plateau-related tectonics (e.g., Burchfiel et al., 1989; Van der Woerd et al., 1998; Mock et al., 1999; Jolivet et al., 2003; Fu and Awata, 2007; Meng and Fang, 2008; Clark et al., 2010). A few researchers have concentrated on quantitative studies of uplift and denudation of the Eastern Kunlun terrain — the main part of the northern Tibet margin using low-temperature thermochronological techniques, e.g., ^{40}Ar/^{39}Ar (Mock et al., 1999; Wang et al., 2004), fission track (Yuan et al., 2006), and (U–Th)/He (Clark et al., 2010; Dai et al., 2013), from which a cooling history of between 40 and 350 °C can be extracted. Based on this cooling history, a rapid cooling event around 30 (Mock et al., 1999; Wang et al., 2004) or 40 Ma (Clark et al., 2010) and therefore the onset time of the initial unroofing of the Eastern Kunlun have been

deduced. This event has been attributed to early uplift (Mock et al., 1999; Wang et al., 2004) or faulting (Clark et al., 2010) induced by Tibet rising. Exhumation rates of between 0.02 and 0.05 mm/yr were reported for the northern part of central segment of the Eastern Kunlun during Late Oligocene–Early Miocene (Dai et al., 2013).

However, direct evidence of couplings between tectonics and surface processes remains elusive, and quantitative data are needed to better constrain denudation evolution and relief history.

A recently developed method for inverse modeling is the one that involves the use of the three-dimensional thermal kinematic model Pecube (Braun, 2002, 2003, Braun et al., 2006), coupled with the Neighbourhood Algorithm (Sambridge, 1999a, 1999b). Pecube is a robust finite-element code to solve the 3D heat transportation equation in a crustal/lithospheric block undergoing uplift and surface erosion, and is characterized by an evolving, finite-amplitude surface topography (Braun, 2003). Following an imposed tectonic scenario, the temperature history of the rocks exhumed at the Earth's surface is derived from the computed crustal thermal structure. These T–t paths can then be used to calculate apparent isotopic ages for a range of geochronometers. The basic set of the Neighbourhood Algorithm is used to find the optimum values of the given parameters of the model that will minimize the misfit function defined by the difference between the observed ages and calculations. The method has been fully described by Braun (2003), Braun et al. (2006) and Valla et al. (2010), and has been successfully applied to the estimation of the denudation and relief history of the Western Alps (van der Beek et al., 2010).

Besides searching for best-fitting model parameters (Braun and van der Beek, 2004; Braun and Robert, 2005; Herman et al., 2007; Valla et al., 2010; van der Beek et al., 2010), the crustal thermal structure (Braun, 2003) was also calculated and Bayesian probability-density functions derived for the parameters estimated (Valla et al., 2010; van der Beek et al., 2010). In this paper, this method was applied to a new (U–Th)/He dataset collected along two transects in the northern Tibet margin (Eastern Kunlun), with the objective of quantifying the crustal thermal structure, and timing of the denudation and relief development of this terrain. This study also provides constraints on mechanical models of orogenic development in northern Tibet, and the far-field effect of rising plateau.

In the following, a brief geological setting of the study area is first presented, followed by the thermochronological study of ^{40}Ar/^{39}Ar and (U–Th)/He. Age–elevation profiles and their conventional implications regarding cooling and exhumation rates through time are evaluated. The modeling approach used in extracting the denudation and relief histories from the data is summarized, and its implications for understanding the tectonic and climatic controls on these histories are discussed.

2. Geological setting and sample collection

The Eastern Kunlun range, stretching for over 1000 km from east to west, delimits the Tibetan Plateau in the south, and the Qaidam Basin in the north (Fig. 1). Being part of the Paleozoic-Triassic collision belt, the Eastern Kunlun was rejuvenated during the Cenozoic Eurasia–Indian collision (Matte et al., 1996), and confined by the South Qaidam Fault in the north and the Kunlun Fault in the south (Fig. 1b, c). The Eastern Kunlun is dominantly composed of pre-Cenozoic plutonic rocks, Devonian to Early Triassic marine sediments, and Jurassic and Cenozoic non-marine rocks (Fig. 1c; Liu et al., 2005; Dai et al., 2013). The plutonic rocks are characterized by widely spread Early Cambrian to Early Devonian (515–393 Ma; Liu et al., 2005; Xiong et al., 2014; Zhang et al., 2010) and Late Permian to Triassic igneous rocks (261–215 Ma; Harris et al., 1988; Ding et al., 2014; Huang et al., 2014; Dai et al., 2013).

The Eastern Kunlun was built during Late Permian to Middle Triassic as a result of northwards subduction of Thethys ocean plate under the Eastern Kunlun and the following collision between Songpan-Ganzi and Eastern Kunlun blocks (Li et al., 2013; Yang et al., 2005). The

Permian toTriassic sediments in the south of the Eastern Kunlun indicate the remnant of foreland basin (Fig. 1), which were reworked intensively by refilling, faulting and folding during Mesozoic and Cenozoic time (Li et al., 2013; Yang et al., 2005).

Two distinct views are advanced for the mechanism of the tectonic regime in northern Tibet: (1) thin viscous sheet model: most of the convergence between India and Asia is expressed in crustal thickening first and then propagated northerly by strike-slip faulting in the shallow crust (England and Houseman, 1986); and (2) synchronous deformation model: initial deformation in the northern Tibet is coeval with the onset of collision between India and Asia under the assumption of a rigid block for the Tibetan Plateau. If the first view is correct, the initiation of the faults, ranges and basins surrounding northern Tibet should be young. Although numerous phenomena do appear along the northern Tibet margin do appear to have been initiated since Miocene, e.g., rapid exhumation around 30 Ma (Mock et al., 1999; Wang et al., 2004), Miocene right-lateral faulting (Wang and Burchfiel, 2004; Fu and Awata, 2007), a mid-Miocene clockwise rotation of the Guide Basin (Yan et al., 2006), U/Pb signatures of mountain building at ~8 Ma (Lease et al., 2007) and Miocene crustal shortening (Bovet et al., 2009), the geological record indicates that the view of initiation and propagation of deformation away from the initial collision boundary may be incorrect (Clark et al., 2010). The depositional and deformation history of sedimentary basins shows that the deformation in numerous localities across northern Tibet could be of Paleocene to Eocene age (Yin et al., 2007; Yin et al., 2008; Meng and Fang, 2008), which roughly coincides with the onset of the continental collision between India and Eurasia (e.g. Rowley, 1996; Wang et al., 2011).

Vertical transects on granite rocks were sampled with minimal horizontal offset where possible. Nine samples in total from two transects were collected for biotite and K-feldspar ^{40}Ar/^{39}Ar dating and apatite (U–Th)/He dating (Fig. 1c). Note that the closure temperatures of biotite and the largest domains in k-feldspar are same (~350 °C, e.g. Lovera et al., 1997, 2002), the ages of biotite and maximum age of k-feldspars from the same sample should be same. These two ages could support one another.

In order to increase representativeness, two transects—50 km from each other, and across the massif between Nuomuhong and Golmud—were sampled (Fig. 1b). Three samples were collected from transect 1, and six from transect 2.

3. Analysis techniques

All samples from the two transects were analyzed by using the modern (U–Th)/He dating technique, while two samples from the top (kl5) and bottom (kl4–2) of transect 1 and three from the top (kl22–2), middle (kl20–2) and bottom (kl18–2) of transect 2 were conducted with the ^{40}Ar/^{39}Ar method. All experiments were carried out in the ^{40}Ar/^{39}Ar and (U–Th)/He Laboratory of the Institute of Geology and Geophysics, Chinese Academy of Sciences (IGGCAS).

The rock samples were first mechanically disintegrated and crushed. Specifically, the coarser shard between 280 and 450 μm and the finer one between 200 and 75 μm in diameter were separated, respectively, from the sample during crushing. K-feldspar and biotite grains free of visible minerals and fluid inclusions were selected by hand under a binocular microscope from the coarser shard, while the apatite crystals were hand-picked from the finer shard.

K-feldspars were carefully checked to match the criteria or requirements for thermochronological study by using the ^{40}Ar/^{39}Ar method (Lovera et al., 1997, 2002; Lee, 1995). For example, the K-feldspar that partially changed to adularia, and/or replaced all earlier microtextures with ultra-porous late feldspar, was eliminated by using electronic microscope probe analyses. To reveal the argon distribution within the K-feldspar grain as finely as possible, the high-resolution (36–40 step) step-heating technique of ^{40}Ar/^{39}Ar analysis was used. Biotite from the same sample was also analyzed for comparison with K-feldspar. Sample
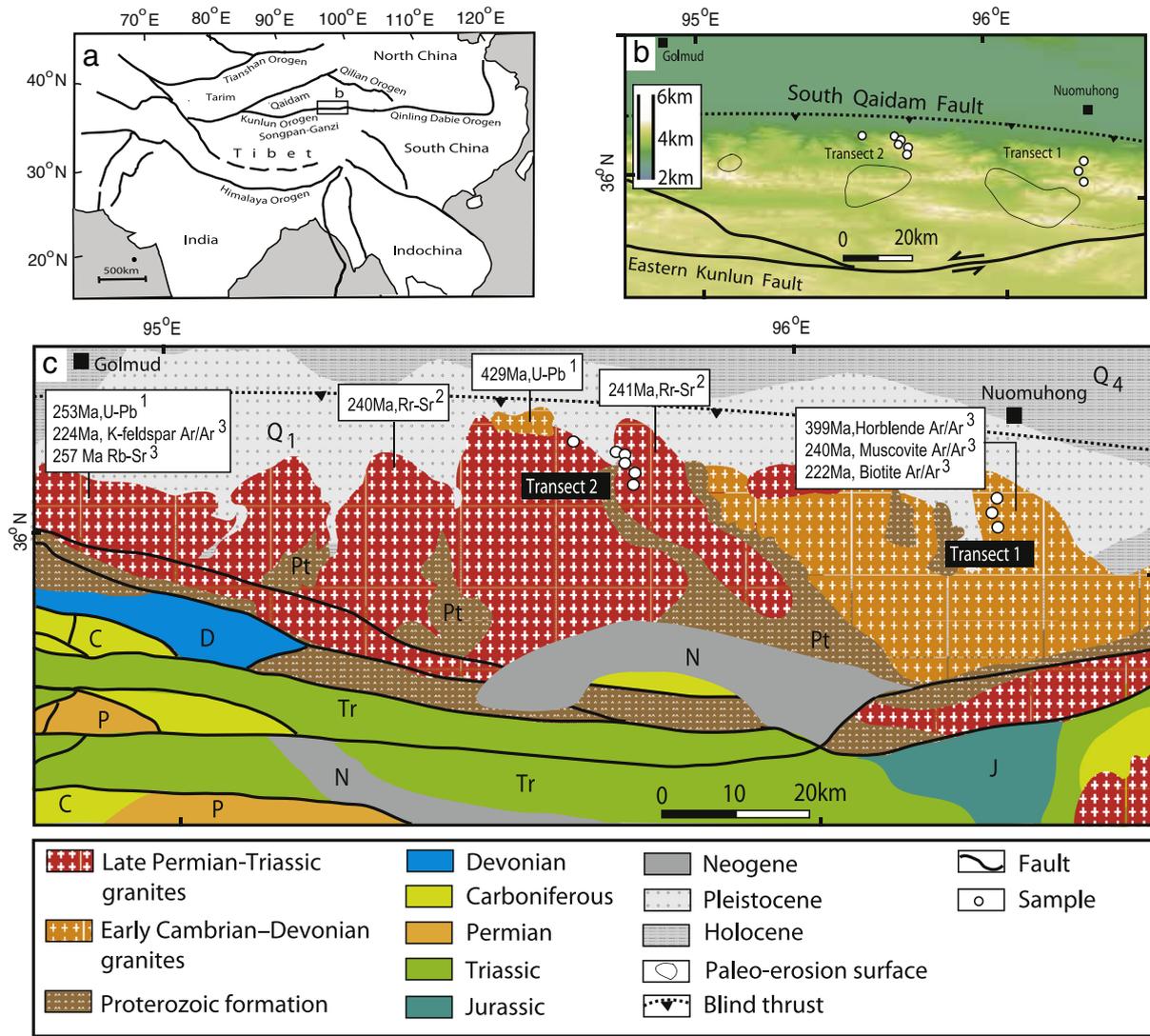
Fig. 1. a) Geological sketch map of Tibet and its adjacent area. b) Topography map of study area showing sample location of Transects 1 and 2. c) Sketched geological map of study area (simplified from BGMR Qinghai, 1991 and Zhang et al., 2014). Ages are from 1) Dai et al., 2013; 2) Harris et al., 1988; 3) Liu et al., 2005 and reference therein.

processing and laboratory procedures of ^{40}Ar/^{39}Ar analysis were depicted in Wang et al. (2007, 2009) and detailed in Appendix A.

Each apatite grain was checked carefully under a high-power microscope in order to exclude those containing impurities and inclusions. Subhedral, fragmentary, needle-like, or rounded apatites were eliminated, as well as apatites with visible zonations. Then, euhedral apatite grains longer than 130 μm and wider than 75 μm were wrapped in a 1 mm × 1 mm platinum capsule and prepared for He, U and Th analyses. He was measured by using an Alphachron MK II noble gas spectrometer, and U and Th on a Thermo Fisher X-Series II ICP-MS. Each of the wrapped apatite grains was moved into a well one after another in a stainless steel disk for He measurement. Each grain was heated twice >1000 °C for 10 min in order to attain complete He extraction. 4He abundance was determined by isotope dilution using a pure 3He spike, calibrated daily against an independent 4He standard tank. The uncertainty in the sample 4He measurement averaged <2%.

The degassed apatite grain was removed from the capsule and placed in a PFA beaker, to which 25 μL of 50% HNO$_3$ with ^{235}U and ^{230}Th spikes were added. A set of reagent blank solutions and spiked U and Th standard solutions were treated similarly. The beaker was gently ultrasounded until the apatite crystal had dissolved. Samples were diluted in 5% HNO$_3$ and analyzed by isotope dilution for U and Th. A detailed description of analytical procedures can be found in Evans et al. (2005a, 2005b). Based on replicate analyses of spiked standard solutions, the analytical precision for ^{235}U/^{238}U and ^{230}Th/^{232}Th was determined to be 0.8% and 0.5%, respectively. (U–Th)/He methods at IGGCAS yielded an internal precision (1σ) of 1.5%, based on multiple age determinations of Durango apatite that produced an average age of 31.5 ± 1.5 Ma (Appendix C), which is well consistent with the recommended age (McDowell et al., 2005; Reiners and Nicolescu, 2006, Evans et al., 2005b).

Age calculation was made by using a Java-based program (Helioplot) (Vermeesch, 2010), and alpha emission correction (Farley et al., 1996) was done by using measured dimensions of each apatite grain. The model described by Gautheron and Tassan-Got (2010).

4. Results of ^{40}Ar/^{39}Ar and (U–Th)/He geochronology

Detailed ^{40}Ar/^{39}Ar and (U–Th)/He analytical results are listed in Appendices B and C, respectively, and are summarized in Table 1 together with the sampling locations and elevations.

Table 1
Sample location and mean apatite (U–Th)/He ages.

Sample	Longitude	Latitude	Elevation (m)	40Ar/39Ar Age (Ma)			(U–Th)/He mean age[a] (Ma)
				Biotite plateau age	k-feldspar plateau age	k-feldspar smallest domain age	
Transect 1							
kl5	96.4635	36.0575	3601	223.3 ± 1.6	224.8 ± 1.2	129.9 ± 4.9	54.1 ± 5.5
kl7	96.4242	36.1046	3446				33.0 ± 3.1
kl4–2	96.4752	36.2186	3224	222.2 ± 1.1	224.4 ± 1.9	138.2 ± 9.2	24.5 ± 2.0
Transect 2							
kl22–2	95.7200	36.2160	4010	224.2 ± 1.2	226.6 ± 1.2	181.8 ± 16.5	82.3 ± 8.6
kl22–3	95.7143	36.2190	3771				63.0 ± 6.7
kl20–2	95.7123	36.2183	3674	223.3 ± 1.2	224.3 ± 1.2	110.3 ± 29.2	66.5 ± 6.4
kl21–3	95.7049	36.2161	3481				40.8 ± 4.1
kl21–1	95.7054	36.2341	3351				36.0 ± 3.5
kl18–2	95.6902	36.2903	3130	222.1 ± 1.2	225.0 ± 1.3	117.1 ± 44.5	32.0 ± 2.9

[a] Calculated from replicate Ft corrected (Farley et al., 1996) single-grain ages Appendix B.

4.1. Results of $^{40}Ar/^{39}Ar$ dating and implications for Mesozoic history of the Eastern Kunlun range

$^{40}Ar/^{39}Ar$ age spectra of K-feldspars and biotites are illustrated in Fig. 2, and the $^{40}Ar/^{39}Ar$ age–elevation relationship is shown in Fig. 3.

All biotite aliquots present flat age spectra with well-defined plateaus accounting for more than 90% of total-released ^{39}Ar (Fig. 2, Appendix B). Biotite plateau ages of samples from the top (kl5) and bottom (kl4–2) of transect 1 are 224.8 ± 1.2 and 224.4 ± 1.9 Ma, respectively, and do not exhibit differences relative to their elevation (Fig. 3, Table 1). Biotite plateau ages of samples, from the top (kl22–2), middle (kl20–2), and bottom (kl18–2) of transect 2, are 226.6 ± 1.2, 224.3 ± 1.2, and 225.0 ± 1.3 Ma, respectively. Although the top sample is slightly older than the other two, they can be taken as "the same" ages if errors are considered (Fig. 2, Table 1). Diffusion loss and distribution of argon isotopes in mineral, which defines the $^{40}Ar/^{39}Ar$ age of the mineral, are closely related to temperature in geological regimes. Thus, the nature of these biotite $^{40}Ar/^{39}Ar$ ages reflects cooling time with a closure temperature of ~350 °C of an exhumation event (e.g., Lovera et al., 1991). The similar ages from the top and bottom of the transects suggest that these vertical transects exhumed and cooled so rapidly that their argon systems were "frozen" at almost the same time (at least they cannot be recognized within errors), giving a cooling time passing the closure temperature of ~350 °C.

K-feldspars usually display complex and variable microstructures usually (Parsons et al., 2013; Cassata and Renne, 2013; Wang et al., 2014) and, as a result, potentially record $^{40}Ar/^{39}Ar$ ages over a range of closure temperatures spanning 200 °C as they cool (Lovera et al., 2002). These microstructures serve as "domains", different in size, in which argon resides, which hold a series of closure temperatures between 350 and 150 °C (Lovera et al., 2002). Thus, K-feldspars represent an important resource for understanding thermal histories (e.g. Lovera et al., 1989, Lovera et al., 1991; Lee, 1995; Cassata and Renne, 2013; Wang et al., 2014). All five k-feldspar samples, from the top, middle, and bottom of the transects 1 and 2 (Fig. 3), exhibit flat age spectra, defining good plateaus accounting for >80% of total released ^{39}Ar at high temperature steps and staircase-shaped age spectra at low temperature steps of step-heating (Fig. 2). The plateau ages rane from 222.1 ± 1.2 to 224.2 ± 1.2 Ma, showing no difference when errors are considered. Moreover, these ages are slightly younger (e.g., kl22–2 and kl18–2) than or "the same as" (e.g., kl5, kl4–2, and kl20–2) their counterpart biotites (Fig. 2a,c,d,e, Table 1) if errors are considered, suggesting that the argon isotopic systems of these k-feldspars were closed at the same temperatures and times as those of biotite (~350 °C). Therefore, the similar ages of k-feldspars from the top, middle and bottom of the studied transects (Fig. 3) suggest that these vertical transects exhumed and cooled rapidly, and

had passed closure temperatures of ~350 °C at the same time around 222.1 to 224.2 Ma.

The age spectra of all k-feldspars at low temperature steps of step-heating exhibit staircase shapes (Fig. 2, Appendix B). Although the low temperature portions account for less than 20% of the total released ^{39}Ar (Fig. 2), the nature (e.g., Lovera et al., 1989, 1991; Cassata and Renne, 2013; Wang et al., 2014) of multi-domains within k-feldspar suggests that these portions potentially reflect slow cooling and recorded cooling ages between ~350–150 °C for transects 1 and 2. All break points are around 220 Ma (Fig. 2), indicating that the time of transition changed from a rapid exhumation to a slow one. The minimum ages are not uniform (Fig. 2) due to analytical limits on the very small amount of argon released, which potentially illustrate the final time passing temperature of ~150 °C. The sample kl-20-2 implies that the slow cooling continued at least to ~110 Ma (Fig. 2d).

In summary, all biotites and k-feldspars show quite consistent $^{40}Ar/^{39}Ar$ flat age spectra, and the k-feldspars indicate some degassing in the beginning of the spectra corresponding with the smallest and less retentive domains. It is consistent with a fast followed by slow exhumation of these samples until probably a depth where the ambient temperature was close to the closure of the smallest domain (e.g., ~150 °C). The $^{40}Ar/^{39}Ar$ geochronology on biotites and k-feldspars of the two transects imply that rocks now at the surface resided around ~350 °C isotherm during the late Triassic and had cooled to ~150 °C by Middle Cretaceous. Note that although ~350 °C mark approximately the closure of both the biotite and the largest domain in K-feldspar, it is a only lower bound of the sample temperature at the initial of exhumation. Therefore, these results pose a minimum bound on total exhumation of ~11.7–14.0 km in the Eastern Kunlun Range, assuming a paleo-geothermal gradient of 30 °C/km (Qiu, 2002) or 25 °C/km (Clark et al., 2010).

4.2. Results of apatite (U–Th)/He dating and implications for the Cenozoic history of the Eastern Kunlun range

The advantage of apatite (U–Th)/He dating arises from its ubiquity and moderately high U and Th content, but more importantly form the fact that He accumulation in apatite occurs only at temperatures below ~75 °C (Wolf et al., 1996); Specifically, diffusion removes He as fast as it is produced by decay at higher temperatures. Therefore, apatite (U–Th)/He dating results document the latest phase of cooling in the uppermost crust (Ketcham et al., 1999).

Typically, three to four grains from each sample were analyzed separately to calculate the mean age in this study (Table 1 and Appendix C). The analysis results (Appendix C) show that more than two grains at least yielded consistent ages for each sample. The scattered older ages of some grains in a sample (e.g., kl5 and kl18–2) may arise from mineral
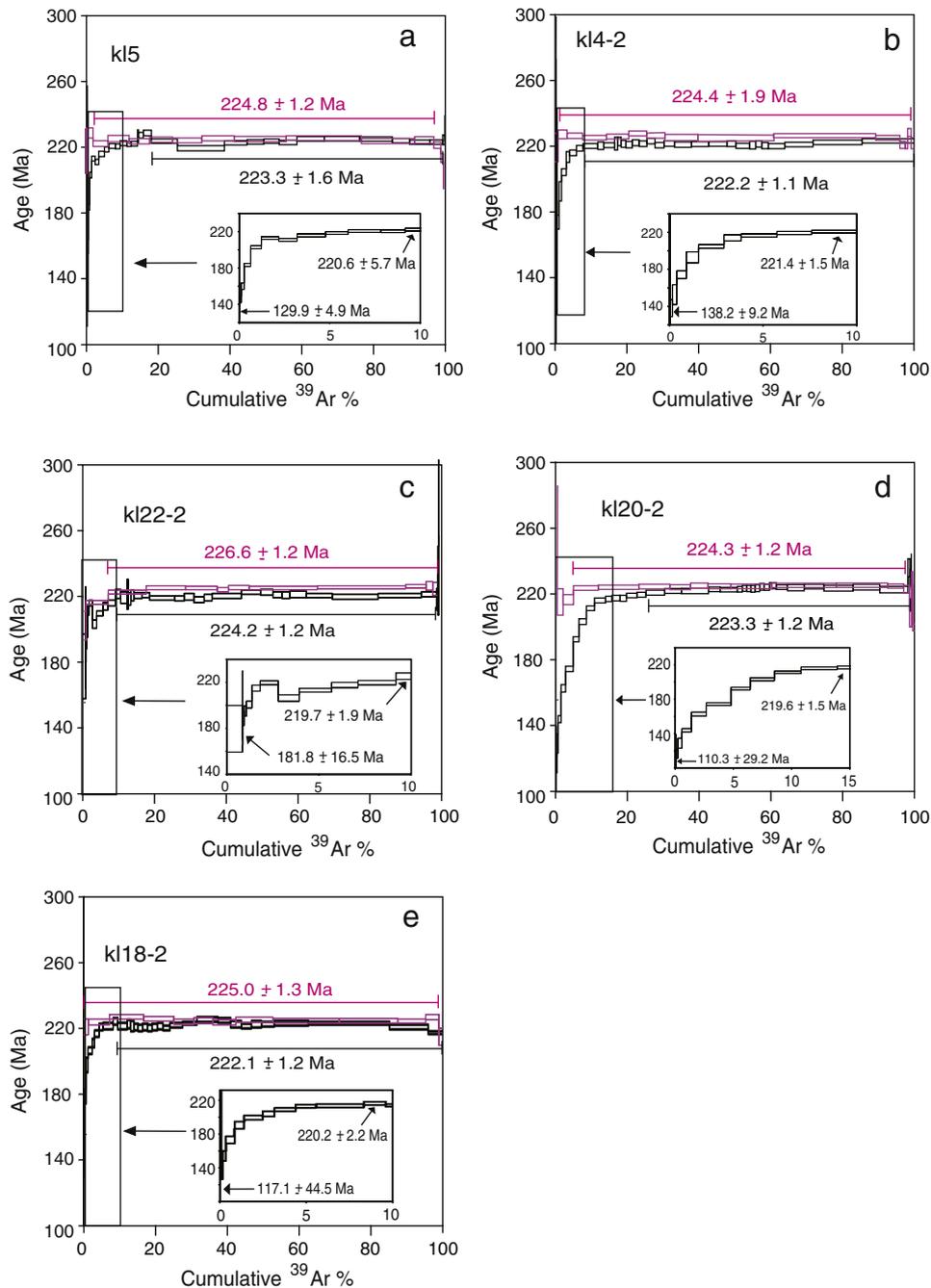
Fig. 2. ^{40}Ar/^{39}Ar age spectra of K-feldspars (black) and biotites (red) from the transects 1 and 2. Plateau ages are shown for K-feldspars at high temperatures and biotite respectively. Insets indicate the staircase age spectra of K-feldspar at low temperatures with its minimum and maximum ages labeled.

inclusions with high U and Th concentrations, especially from zircon and monazite (Ehlers and Farley, 2003) which produce erroneously high He age in some apatites. Although careful microscopic examination of grains to be dated greatly reduces this problem (Farley, 2002), some inclusions may be too small to detect (Ehlers and Farley, 2003). Fortunately, inclusions tend to be heterogeneously distributed from grain to grain, causing poor age reproducibility. Thus, age reproducibility is an indispensable demonstration of the quality of an apatite He age.

Good age reproducibility between grains (Appendix C) indicates that our new (U–Th)/He ages are reliable. Three samples from transect 1 yield ages of 54.1 ± 5.5, 33.0 ± 3.1 and 24.5 ± 2.0 Ma from top to bottom, showing a positive correlation with elevation (Fig. 4). Similarly, six samples from transect 2 give ages of 82.3 ± 8.6, 63.0 ± 6.7, 66.5 ± 6.4,

40.8 ± 4.1, 36.0 ± 3.5, and 32.0 ± 2.0 Ma from top to bottom, consistent with the trend of elevation (Fig. 4).

Considering that there is no fault between the transects 1 and 2 (Fig. 1), which may cause differential movement, it can be assumed that the plutons of transects 1 and 2 were exhumed uniformly, and no different amounts of fault throw along strike of the South Qaidam fault. This is an acceptable assumption based on our new ^{40}Ar/^{39}Ar geochronological results above. Moreover, several regional erosion surfaces preserved at an elevation of ~4600 m throughout the study area were recognized from a 60-m-resolution digital elevation model (DEM)(Fig. 1), and they do not show any local tilting. This means that there is no influence from long-wavelength undulations in the geomorphic surface. Therefore, it is reasonable to directly integrate transects 1 and 2 to form
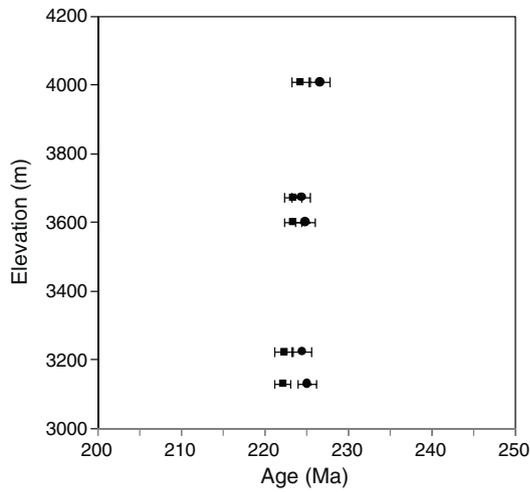
Fig. 3. $^{40}Ar/^{39}Ar$ age–elevation relationship. Solid square denotes the ages of K-feldspars and solid circle represents the ages of biotites.

a uniform age–elevation relationship (AER) and discuss them together (Fig. 4).

(U–Th)/He ages record cooling commonly caused by exhumation, i.e., rock motion towards the surface of the Earth. In other words, what processes produced exhumation and when and how fast they operated can be illustrated by (U–Th)/He dating. Usually, these issues are approached by establishing the (U–Th)/He age distribution with increasing elevation or paleodepth (e.g., Ehlers and Farley, 2003). In most cases crustal temperatures increase and (U–Th)/He ages decrease with depth, but the exact pattern of variability depends on the specific exhumation history (Ehlers and Farley, 2003).

In Fig. 4, the overall pattern of the age–elevation curve of this study shows two distinct segments: from ~80–40 Ma ages decrease approximately linearly with elevation suggesting that rock had experienced a constant exhumation rate at which the He age pattern reached a steady state. A striking increase in the slope during ~40–~30 Ma (Fig. 4), however, suggests an increase of exhumation rate, or a rapid cooling event at ~40 Ma. This pattern of age–elevation curve is consistent with one-dimensional cooling and age–depth relationship (e.g. Ehlers and Farley, 2003), as implied by the discussion above.

The transition from the gentle to the steeper slope occurred at ~3500 m elevation, which can be considered to be the position of the paleo-closure isotherm of ~40 Ma. This implies that a 2.0–2.3 km thick
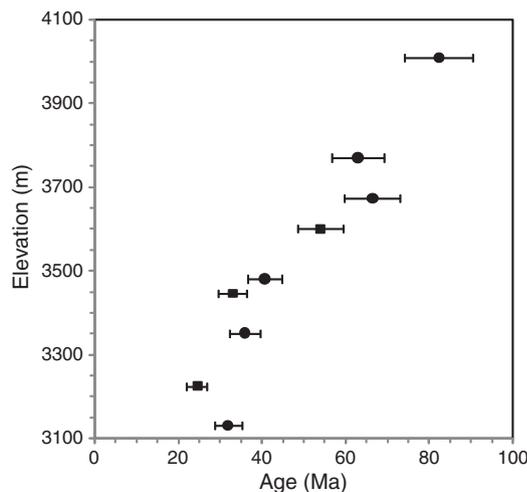

Fig. 4. (U–Th)/He age–elevation relationship (AER). Solid square denotes the samples of transect 1 while solid circle represents the samples from transect 2.

overburden could have been removed from the Eastern Kunlun Range since 40 Ma, given geothermal gradients measured in the Qaidam Basin (30 °C/km) for Cenozoic (Qiu, 2002), surface temperature (10 °C), and a range of He closure temperatures (60–70 °C), yielding a range of denudation rate of 0.05–0.058 mm/yr.

Tectonically, the sudden increase in age–elevation gradient implies that rapid exhumation could have occurred at ~40 Ma, which may be related to a rapid uplift event under favorable climatic conditions. The uplift induced increase of erosion and exhumation, and thus samples beneath the closure isotherm moved upwards through the isotherm at almost the same time.

In order to constrain the evolution history of relief and denudation accurately, quantitative analysis by thermal modeling on thermochronological data is needed.

5. Thermal modeling of age–elevation data

5.1. Pecube coupled with Neighbourhood Algorithm (NA)

In nature being a forward model to predict cooling history and age, Pecube, coupled with NA, can be used for back-calculating the parameters concerning the geological past.

Pecube devotes to the case of "temporally-changing" surface topographical effect on the thermal structure of the underneath crust by solving the following transient, three-dimensional heat transfer equation (Carslaw and Jaeger, 1959; Braun, 2003):

$$\rho c \left(\frac{\partial T}{\partial t} + \upsilon \frac{\partial T}{\partial z} \right) = \frac{\partial}{\partial x} \kappa \frac{\partial T}{\partial x} + \frac{\partial}{\partial y} \kappa \frac{\partial T}{\partial y} + \frac{\partial}{\partial z} \kappa \frac{\partial T}{\partial z} + \rho A, \quad (1)$$

where T(x,y,z) is the temperature, ρ is the rock density, c is the heat capacity, υ is the vertical rate of rocks relative to the base of the crust, κ denotes the conductivity and A is radioactive heat production. This equation must be solved for a set of boundary conditions. For ease of use, some assumptions have been made including that thermal properties such as rock conductivity, heat capacity, density and heat production are spatially uniform and constant through time. A full description of the numerical method is provided in Braun (2003).

The inverse calculation was implemented by using the Neighbourhood Algorithm (NA) (Sambridge, 1999a, 1999b). NA involves an iterative search in the multi-dimensional parameter space in order to find sets of input parameters that minimize the misfit between observed and predicted data normalized by the squares of the errors:

$$\psi = \sqrt{\sum_{i=1}^{N} \sum_{j=1}^{M} \frac{^{i}\alpha_{j.mod} - ^{i}\alpha_{j.dat}}{^{i}\sigma_{j}}} \quad (2)$$

where N denotes the number of datasets, M is the number of sample of samples in each dataset, $^{i}\alpha_{j.mod}$ and $^{i}\alpha_{j.dat}$ are the predicted and observed valuse respectively, and $^{i}\alpha_{j}$ is the error on the data (Valla et al., 2010; van der Beek et al., 2010).

5.2. Modeling: results and evaluations

The input thermo-kinematic parameters used in Pecube are listed in Table 2. The geometry of the surface topography was extracted from 1-km-resolution DEMs (GoodyGIS). Changes in relief were incorporated by only modifying the amplitude of topography but not the shape of the relief as designed by Braun (2003). This assumption requires incision mainly occurred in valley and geometry of the drainage system did not change over the time span modeled. This assumption may not always satisfy the geological situation, but the long standing peak and valley and incision mainly confined in valleys in a region suggest the assumption acceptable (Braun and van der Beek, 2004; Braun and Robert, 2005; Valla et al., 2010 and van der Beek et al., 2010). The Eastern

Table 2
Thermo-kinematic and elastic parameters used in Pecube. Poisson ratio, Young's modulus and equivalent elastic thickness are used for calculating the isostatic rebound in response to relief change. Equivalent elastic thickness is set to a value that simulates moderate isostatic rebound.

Parameter	Value
Crustal thickness (km)	60
Crustal density (kg/m^{-3})	2700
Sublithospheric mantle density (kg/m^{-3})	3200
Equivalent elastic thickness (km)	25
Young's modulus (Pa)	1.1^{11}
Poisson ratio	0.25
Thermal diffusivity (km^2/Myr)	25
Sea level temperature (°C)	15
Atmospheric lapse rate (°C/km)	0
Crustal heat production (°C/Myr)	0

Kunlun has served as provenance for the Qaidam basin from Late Mesozoic to the present time constantly, as indicated by the sedimentary sequence (Meng and Fang, 2008; Guan and Guan and Jian, 2013), implying the surface runoff system did not change significantly during Mesozoic although the amplitude of topography may keep changing.

He diffusion kinetics from Farley (2000) (Durango apatite) were used in the Pecube calculation of cooling history and theoretical (U–Th)/He ages (Braun, 2003). Modeling calculation was implemented at the MPI Computation Laboratory of IGGCAS.

In order to investigate different possibilities of evolutionary history for the Eastern Kunlun, two scenarios were modeled: Scenario 1, a constant exhumation rate from a high relief over the past 100 Ma, and Scenario 2, variable exhumation rate and relief over the past 100 Ma. In our conceptual model, we assume that relief increases from preferential valley incision, i.e., the shape of the topography is constant spatially over the modeling time span.

Inversion modeling results for Scenarios 1 and 2 are shown in Figs. 5 and 6, respectively, in which each dot represents a forward model. The misfit function ψ allows for a direct comparison of inversion runs with different numbers of data. For this study, the models represented by

misfit values <0.5 were considered "satisfying", as shown by the color of each dot (Fig. 5, 6).

Scenario 1 assumes a one stage denudation and relief evolution history, in which the Eastern Kunlun was initially built high and exhumated completely during later Paleozoic and early Mesozoic, and constantly eroded over the past 100 Ma; Moreover, reactivation caused by the Cenozoic collision between India and Eurasia did not affect the relief of Kunlun terrain. Modeling ran over 100 Ma to ensure that all points, which end up at the surface, cool through the AHe closure temperature. Only one phase (100–0 Ma) was modeled. The relief factor (R) was set between 0 and 2, denudation rate (D) between 0 and 2.0 mm/yr and paleo-thermal gradient (T) between 15 and 30 °C/km. The relief factor is defined by Valla et al. (2010) as:

$$R = \Delta h_i / \Delta h_0 \tag{3}$$

where Δh_i is the maximum difference of height in the study area at i stage, and Δh_0 is the present maximum difference of height.

5000 forward models were calculated for Scenarios 1 (Fig. 5). The minimum misfit values of the "best" forward models are around 0.623 (Fig. 5) which is slightly bigger than the "satisfying value (0.5)". The distribution of the forward modes are not convergent (Fig. 5), and therefore do not resolve a unique set of parameters for relief evolution (R = 0–2.0), denudation rates (D = 0–2.0 mm/yr) and paleo-thermal gradient (T = 15–30 °C/km). Although the paleo-thermal gradient of change is constrained in a relatively small range of 17–20 °C/km, the denudation rate and relief factor are sinuous in a wide range of ~0.06–~0.7 mm/yr and ~0.2–~1.5 respectively (Fig. 5). Therefore, the modeling results for Scenario 1 suggest that the assumptions of a one-stage history over the past 100 Ma for the Eastern Kunlun are unreasonable.

Scenario 2 assumes a multiple stage of denudation and relief evolution history, in which. Relief of Kunlun terrain was rebuilt by the effect of the collision. In order to reflect the rejuvenation of the Eastern Kunlun during the Cenozoic Eurasia–Indian collision, the modeling including three phases (100–50, 50–40 and 40–0 Ma) with seven associated parameters: (1) relief factor (R$_1$: 0–2.0) and denudation rate (D$_1$: 0–2.0 mm/yr) during the first stage; (2) relief factor (R$_2$: 0–2)and denudation rate (D$_2$: 0–2.0 mm/yr) during the second stage; (3) relief factor
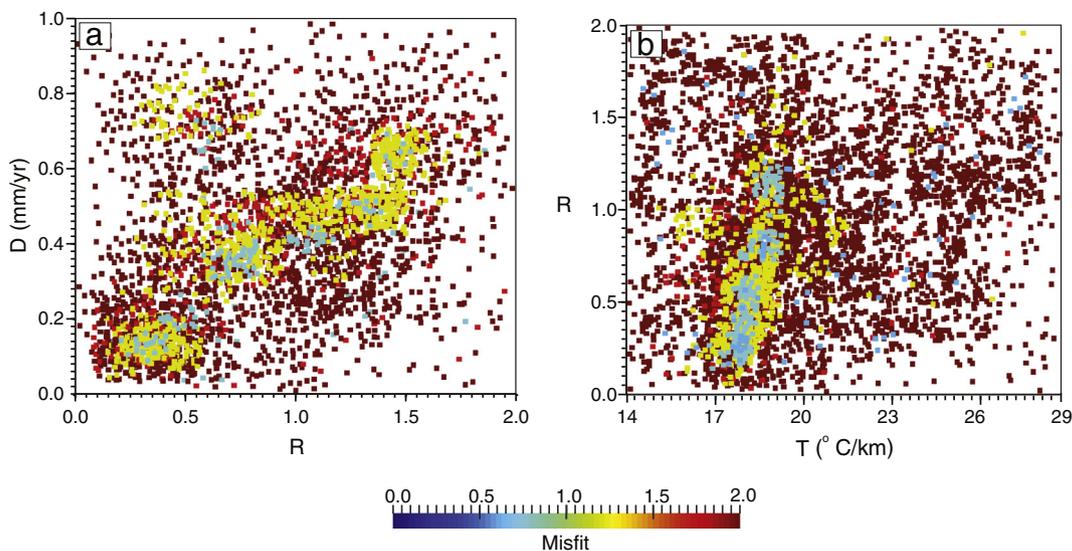

Fig. 5. Scatter plots showing results of Pecube + NA inversion for Scenario 1. Each dot denotes a forward model, and its color corresponds to the value of color bar for misfit between modeled and input data. Blue corresponds to misfit value <0.5. Each plot is the projection onto a plane by two of the seven parameters (denudation rates D; relief factor R; and thermal gradient T). Horizontal and vertical axes define the parameter space. The results are not convergent and not a unique set of parameters can be determined implying assumptions for Scenario 1 are unreasonable and infeasible. (For interpretation of the references to color in this figure legend, the reader is referred to the online version of this chapter.)
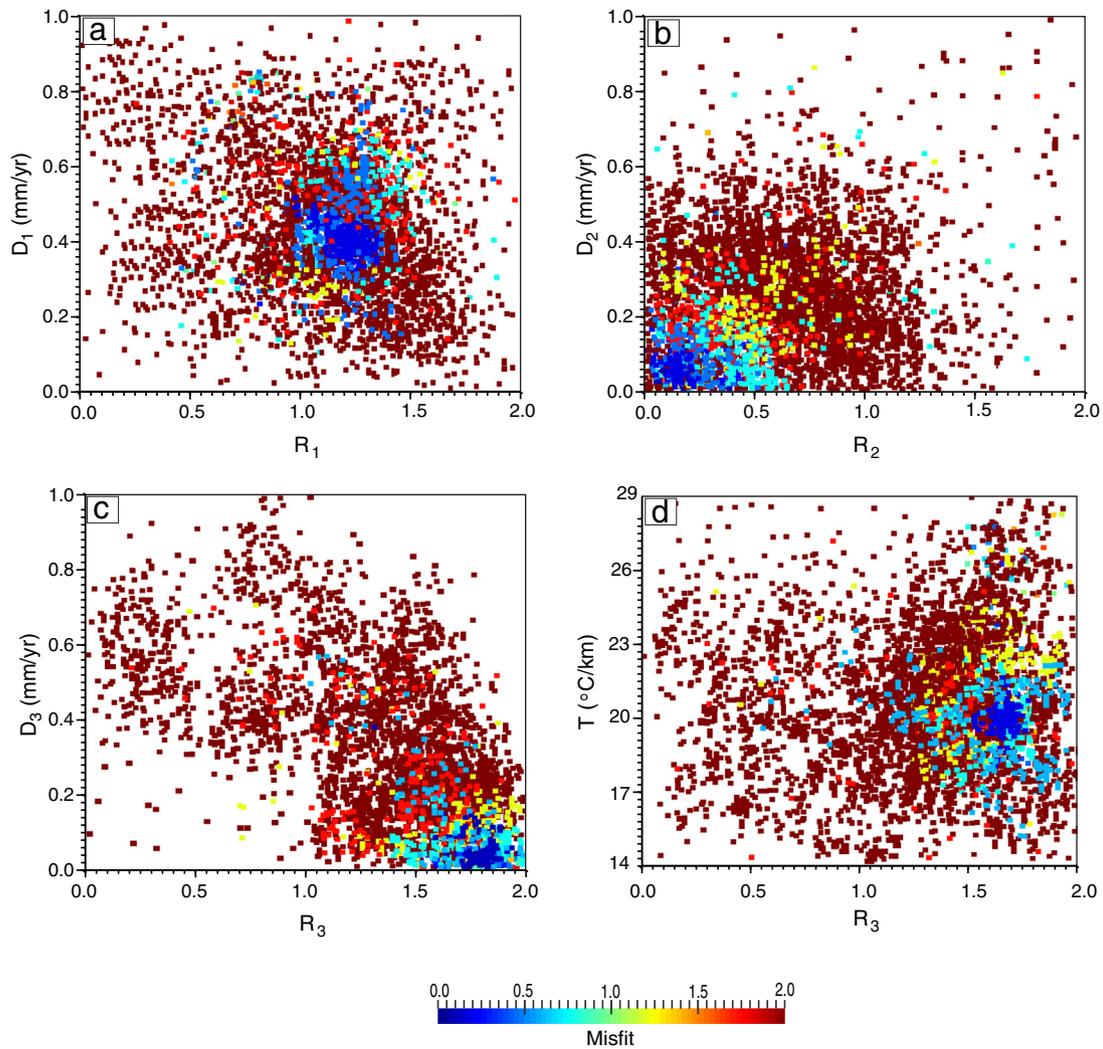
Fig. 6. Scatter diagrams showing results of Pecube + NA inversion for Scenario 2. Same plots as Fig. 5 but seven parameters (denudation rates D1, D2, D3; relief factor R1, R2, R3; and thermal gradient T); horizontal and vertical axes define the parameter space. The results converge and a unique set of parameters can be determined, implying assumptions for Scenario 2 are reasonable and reflect the "real" situation.

(R_3: 0–2) and denudation rate (R_3: 0–2.0 mm/yr) during the third stage; geothermal gradient (T: 15.0–30.0 °C/km).

8500 forward models were calculated for Scenarios 2 (Fig. 6). The minimum misfit values of the "best" forward models are around 0.051 (Fig. 6) which is much better than the "satisfying value (0.5)". The distribution of the forward modes is converge well as shown in Fig. 6, and a set of parameters for three stages of denudation rates (D_1, D_2, D_3), relief factors (R_1, R_2, R_3) and paleo-thermal gradient (T) are well resolved (Fig. 6). This means that the assumptions of multiple stages of denudation and relief evolution history are feasible for the Eastern Kunlun Belt over the past 100 Ma.

From graphical inspection of Fig. 6, it is further found that the optimum values for these parameters are constrained in small ranges: D_1 in 0.3–0.45 mm/yr, D_2 in 0–0.05 mm/yr and D_3 in 0.04–0.11 mm/yr, R_1 in 1.25–1.58, R_2 in 0.1–0.3, R_3 in 1.7–2.0 and T in 19.4–21.1 °C/km.

By investigating the statistical properties of the model ensemble using probability density function (PDF), the most probable values for the parameters can be obtained (Fig. 7, Table 3) and the uncertainty can be defined by the standard deviation of the marginal PDF. Parameter PDFs confirm three contrasting stages for the exhumation history: (1) high denudation rates ($D_1 = 0.37 \pm 0.27$ mm/yr, Fig. 7b) at 100 Ma; (2) low denudation rates ($D_2 = 0.013^{+0.025}_{-0.013}$ mm/yr, Fig. 7b) at 50 Ma; and (3) higher denudation rate ($D_3 = 0.052 \pm 0.025$ mm/yr, Fig. 7b) at 40 Ma and the present. Relief history is even more precisely

constrained: $R_1 = 1.38 \pm 0.21$ (Fig. 7a) at 100 Ma; $R_2 = 0.17 \pm 0.14$ at 50 Ma (Fig. 7a); and $R_3 = 1.82 \pm 0.21$ at 40 Ma (Fig. 7a). Thermal gradient is also well constrained as 20.6 ± 2.1 °C/km (Fig. 7c), not changing for the three stages. AER implies apparent erosion rates <0.2 mm/yr for several tens of millions years, which suggests that the changes in geothermal gradient due to heat advection from erosion were minor (Moore and England, 2001; Ehlers, 2005; Clark et al., 2010). The changes of relief history with time are graphically shown in Fig. 8 as 3D perspective plots.

The modeled denudation rates are similar to those inferred directly from the inspection of AER: $0.013^{+0.025}_{-0.013}$ (modeled) vs ~0.012 mm/yr (AER) at 50 Ma and 0.052 ± 0.025 (modeled) vs 0.05–0.058 mm/yr (AER) at 40 Ma. The modeled geothermal gradient (20.6 ± 2.1 °C/km) is similar to the previous observations for the Eastern Kunlun (25 °C/km) (Clark et al., 2010) and the Qaidam Basin (20–30 °C/km) (Qiu, 2002).

Best-fit Scenario 2 yields the predicted age–elevation relationship reasonably well compared with the observed (Fig. 8). The thermal histories for each sample predicted by the Pecube show similar cooling and exhumation pattern (Fig. 9) to the observations from the AER in Fig. 4: a rapid cooling or exhumation stage between ~40 and ~30 Ma and a relative slow cooling or exhumation from ~100 to ~50 Ma (Fig. 9). The thermal history roughly passes the minimum 40Ar/39Ar ages of k-feldspar (Fig. 9), implying that the cooling or exhumation
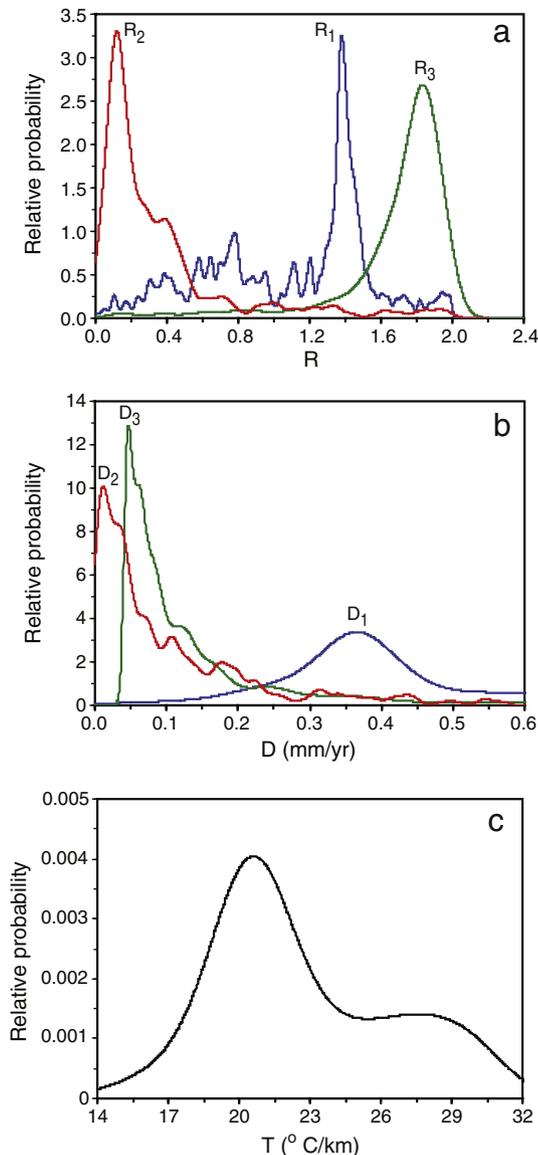
Fig. 7. The probability density function (PDF) results for the "most probable" parameters for Scenario 2: a) relief factors for the three stages; b) denudation rates for the three stages; c) thermal gradient.
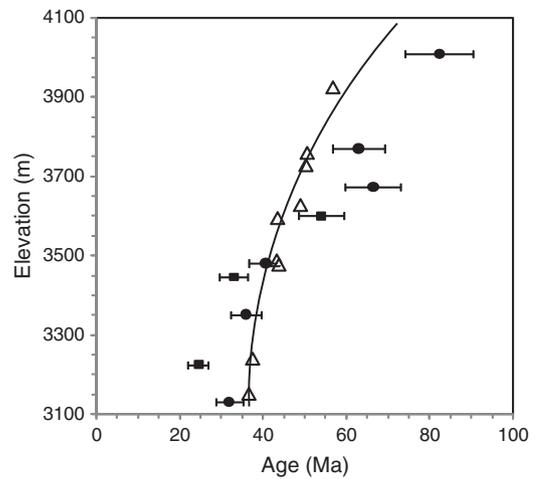

Fig. 8. Comparison of predicted (white triangles) and observed (black squares and circles). The solid line gives trend of the modeled. Predicted data are from the "most probable" values.

compressed towards the surface and deformed by the high relief surface topography (e.g., Fig. 10c).

6. Implications for evolution of the Northern Tibet margin and the far-field effect of rising plateau

6.1. Denudation evolution and relief history of the Northern Tibet margin

Our new $^{40}Ar/^{39}Ar$ dating on k-feldspar and biotite from the studied transects suggests that the Eastern Kunlun terrain exhumated and cooled rapidly in the later Triassic (~220 Ma), and implies a total exhumation of ~11.7–14.0 km since then, assuming a paleo-geothermal gradient of 30 °C/km (Qiu, 2002) or 25 °C/km (Clark et al., 2010). New (U–Th)/He dating in this study indicates constant and slow exhumation during ~80–40 Ma, and a rapid cooling event at ~40 Ma.

Inversion modeling results show that the relief decreased from ~100 to ~50 Ma, increased from ~50 to ~40 Ma, and then decreased again from ~40 to the present (Fig. 10). Being a part of the Paleozoic-Triassic collision belt, the Eastern Kunlun was unroofed during ~100–50 Ma, resulting in the decrease of the relief factor from 1.38 ± 0.21 at 100 Ma to 0.17 ± 0.21 at 50 Ma (Fig. 10a,b); meanwhile, the denudation rates decreased sharply from 0.37 ± 0.27 to $0.013^{+0.025}_{-0.013}$ mm/yr (Fig. 10a,b). This possibly suggests that the crust was in a quiet or stable tectonic setting during ~100–50 Ma. Therefore, unroofing constituted the first order tectonic movement at the northern Tibet margin during this period, when high relief areas were denuded and low relief areas infilled, resulting in a low topography by ~50 Ma (Fig. 10c). From ~50 to ~40 Ma, the relief increased more than tenfold from a factor of 0.17 ± 0.21 to 1.82 ± 0.21 (Fig. 10b,c), with denudation rates increasing from $0.013^{+0.025}_{-0.013}$ to 0.052 ± 0.025 mm/yr, due to the rapid uplift of the Eastern Kunlun terrain spanning 50–40 Ma. Since 40 Ma, the highest relief decreased by almost half, from a factor of 1.82 ± 0.21 to 1.0 at present (Fig. 10c,d), suggesting that the crust was relatively stable and denudation was the main tectonic setting. Rapid uplift of the mountain ranges at the northern Tibet margin accentuated valley incision that led to the formation of foreland flexural depressions, such as the Qaidam
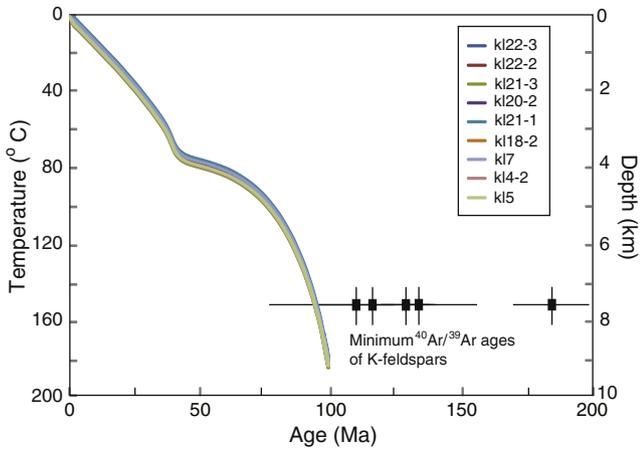
history extracted from (U–Th)/He ages is consistent with what reflects by 40Ar/39Ar k-feldspar smallest domains (see discussion above).

In summary, our modeling results are reasonable and reflect the "actual" situation. The model results can therefore be used to infer a regional exhumation and relief history from the data set. However, potential improvements to our modeling could be provided by more sophisticated age-prediction models or more realistic evolution scenarios.

Graphically 3D plots of the relief and denudation history of different stages over the past 100 Ma are illustrated in Fig. 10. Modeled thermal structures beneath the Eastern Kunlun terrain at different times are illustrated on the sides of the 3D plots. Contours of the temperature field have been superimposed (Fig. 10). The contours of temperature show the effect of vertical heat advection, where the isotherms are

Table 3
Values of parameters of input and modeled.

	R_1	R_2	R_3	T (°C/km)	D_1 (mm/yr)	D_2 (mm/yr)	D_3 (mm/yr)
Input	0–2	0–2	0–2	15–30	0–2.0	0–2.0	0–2.0
Model	1.38 ± 0.21	0.17 ± 0.14	1.82 ± 0.21	20.6 ± 2.1	0.37 ± 0.27	$0.013 + 0.025/-0.013$	0.052 ± 0.025

Fig. 9. Thermal histories for nine samples predicated by Pecube. Temperature transfers to depth using thermal gradient value of 20 °C/km. Five minimum $^{40}Ar/^{39}Ar$ ages (smallest domain ages) of K-feldspars are also shown for comparison.

and Kumkuli Basins. Consequently, increasing denudation rates could have resulted in increased sedimentation rates in the basins.

The results of (U–Th)/He AER and inversion modeling have important implications for deciphering the orogenic development of the northern Tibet margin. AER from the two transects suggest that a rapid denudation/exhumation event occurred around 40 Ma (Fig. 4)

after the Eurasia–Indian collision at ~50 Ma (Rowley, 1996). This is confirmed by the results of inversion modeling, which show that the denudation rate at 40 Ma and present is 0.052 ± 0.025 mm/yr (Fig. 10c,d). This is much higher than the denudation rate of 0.013 ± 0.025 mm/yr during ~50–40 Ma (Fig. 10b). Our new data of (U–Th)/He ages on the Central Kunlun and the Qimen Tagh Mountains, and Miocene growth strata in the Kumukuli Basin, in the range of 39.5–43.2 Ma (authors' paper under preparation), suggest that the rapid exhumation event was widespread throughout the Eastern Kunlun Range. Exhumation of the Central Kunlun Range between 41 and 21 Ma is inferred from accelerated cooling determined from feldspar multi-domain diffusion modeling (Mock et al., 1999; Wang et al., 2004). Previous (U–Th)/He data revealed a rapid exhumation event during 30–45 Ma in the Eastern Kunlun and the Western Qinling Mountains (Clark et al., 2010).

Sedimentation rates in the adjacent Qaidam Basin increased rapidly during 40–36.6 Ma (Me'tivier, 1996; Cui et al., 1999; Chen et al., 1998; Wang et al., 2004), implying an increase of denudation rate in the surrounding mountains. Growth strata are extensively preserved from 50 to 40 Ma in the peripheral areas of the Qaidam and Kumkuli Basins (Bally et al., 1986; Meng and Fang, 2008; Yin et al., 2008). In HoXil basin, immediately south of the study area, there was rapid sedimentation around 40 Ma (Wang et al., 2008).

Denudation or exhumation is a result of the combination of climate and tectonic uplift. Moreover, uplifted high land is preferentially subjected to erosion in a moist and hot climate. It is inferred that the denudation rates of the East Kunlun terrain increased from ~50 to 40 Ma implying that the terrain had been uplifted during this period, when
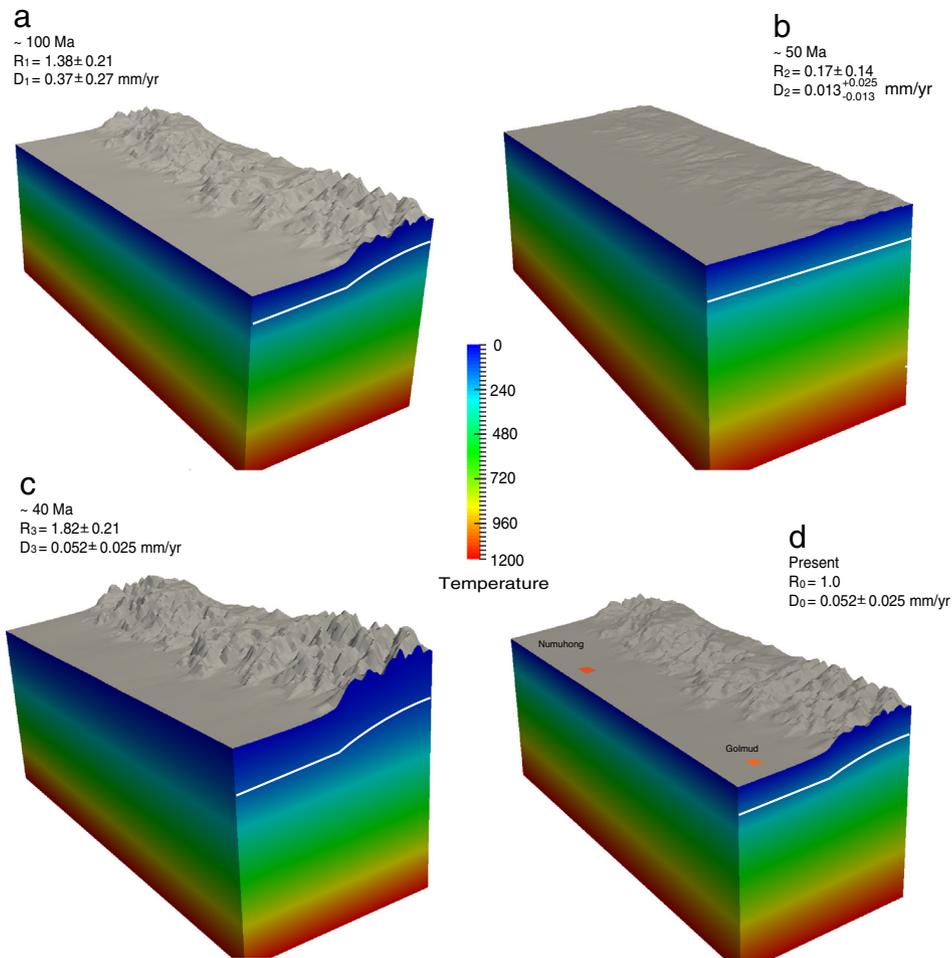

Fig. 10. Perspective view of inversed relief history with temperature field contoured on sides. a) ~100 Ma ($R_1 = 1.38 \pm 0.21$, $D_1 = 0.37 \pm 0.27$), b) ~50 Ma ($R_2 = 0.17 \pm 0.14$, $D_2 = 0.013^{+0.025}_{-0.013}$), c) ~40 Ma ($R_3 = 1.82 \pm 0.21$, $D_3 = 0.052 \pm 0.025$), d) present ($R_0 = 1.0$, $D_0 = 0.052 \pm 0.025$). The contours of temperature show the effect of vertical heat advection especially at ~40 Ma (c, white solid line), where the isotherms are compressed towards the surface and deformed by the high relief surface topography (shown by solid white lines).

favorable climatic conditions were prevailed. Recent data of magnetostratigraphy, pollen, and climatic proxies in northern Tibet and neighbouring areas show that the Eocene–Oligocene Boundary (~34 Ma) marks one of the most pronounced climatic changes of the Cenozoic era, implying the dramatic shift of a "greenhouse" to an "icehouse" world (Wang et al., 2003; Graham et al., 2005; Dupont-Nivet et al., 2007; Clark et al., 2010; Sun et al., 2014). The prevalence of a "greenhouse" climate, which is moist, hot and denudation-friendly, is attributed to the existence of the Parathethys Sea in the south, before the early rise of mountain ranges in northern Tibet. The rising land was denuded mainly by incising valleys (Clark et al., 2010), giving rise to the highest relief at the northern Tibet margin during Cenozoic at ~40 Ma.

6.2. Implications for the far-field effect of rising Tibet

How does the rising Tibetan Plateau affect the far-northern peripheral area? Two contrasting models are proposed in this regard: (1) northerly propagating strain from the collision boundary between India and Eurasia (e.g., England and Houseman, 1986); and (2) synchronous deformation with the onset of collision (e.g. Wang et al., 2008; Clark et al., 2010). The data obtained from this study favors the second model and suggest that the northern Tibet margin was built-up in the early phase of India-Eurasia collision history.

Rapid exhumation and the highest relief at ~40 Ma suggest that the Eastern Kunlun Range was rejuvenated during 50–40 Ma, as an immediate response to the Eurasia–Indian convergence at ~50 Ma (Rowley, 1996), although the plate boundary was located more than 3000 km away to the south. A growing body of evidence indicates that large-scale deformation began across the eastern and central portions of northern Tibet (Rowley, 1996; Clark et al., 2010) within 10 Ma of the collision between India and Eurasia (41–52 Ma). In other words, the north margin of Tibet was built during the early phase of collision history. A decreasing relief and increasing denudation rate, from ~40 Ma to the present, suggest that unroofing was the first-order activity, implying that uplift was minor and northern Tibet has been rather stable since ~40 Ma. Despite 2000–3000 km of convergence of India and with Eurasia since the collision (Molnar and Stock, 2009; Clark et al., 2010), the northerly propagation of strain was insignificant during the entire period of collision. A stable boundary that was built-up at the time of collision cannot be interpreted by the existing indenter models (e.g. Tapponnier et al., 2001) of continental convergence into a uniform lithosphere; instead, it may be better explained by emphasizing the role of strong heterogeneities in the continental lithosphere or basal tractions induced by mantle flow (Clark et al., 2010).

7. Conclusions

A new $^{40}Ar/^{39}Ar$ and apatite (U–Th)/He dataset from transects of the eastern range indicates a minimum exhumation of ~11.7–14.0 km since ~220 Ma, and a rapid exhumation event along the Eastern Kunlun Range at ~40 Ma, following a long period of slow cooling from late Mesozoic to early Eocene. This process possibly prevailed all along the northern Tibet margin and was marked by sedimentation in basins, rapid cooling of mountains and faulting. Inversion modeling of a multiple stage scenario, which elucidates the entire denudation and relief evolution from ~100 Ma to the present, suggests that the highest relief was built-up at ~40 Ma. Since then, denudation has been the first-order activity leading to decreased relief until the present, implying that the northern Tibet margin was relatively stable over the past 40 Myr. The existing northern Tibet margin was built-up during the early phase of the collision history, and the northward propagation of continued convergence between India and Eurasia is not significant. This may be attributed to the strength of heterogeneities in the continental lithosphere or the basal traction induced by mantle flow.

Supplementary data to this article can be found online at http://dx.doi.org/10.1016/j.tecto.2016.03.001.

References

Bally, A., Mingchou, I., Clayton, R., Heugster, H., Kidwell, S., Meckel, L., Ryder, R., Watts, A.B., Wilson, A., 1986. Notes on sedimentary basins in China. Reports of the American Sedimentary Basins Delegation to the People's Republic of China: U.S. Geol. Surv., pp. 86–327 (Open File Rep, 108 p)

Beaumont, C., Fullsack, P., Hamilton, J., 1992. Erosional Control of Active Compressional Orogens. In: McClay, K.R. (Ed.), Thrust Tectonics. Chapman and Hall, London, pp. 1–18.

Bovet, P.M., Ritts, B.D., Gehrels, G., Abbink, A.O., Darby, B., Hourigan, J., 2009. Evidence of Miocene crustal shortening in the North Qilian Shan from Cenozoic stratigraphy of the western Hexi Corridor, Gansu Province. China. Am. J. Sci. 309, 290–329.

Braun, J., 2002. Quantifying the effect of recent relief changes on age–elevation relationships. Earth Planet. Sci. Lett. 200, 331–343.

Braun, J., 2003. Pecube: a new finite element code to solve the heat transport equation in three dimensions in the Earth's crust including the effects of a time-varying, finite amplitude surface topography. Comput. Geosci. 29, 787–794.

Braun, J., Robert, X., 2005. Constraints on the rate of post-orogenic erosional decay from low-temperature thermochronological data: application to the Dabie Shan, China. Earth Surf. Process. Landf. 30, 1203–1225.

Braun, J., van der Beek, P.A., 2004. Evolution of passive margin escarpments: what can we learn from low-temperature thermochronology? J. Geophys. Res. 109, F04009. http://dx.doi.org/10.1029/02004JF000147.

Braun, J., van der Beek, P.A., Batt, G., 2006. Quantitative Thermochronology — Numerical Methods for the Interpretation of Thermochronological Data. Cambridge University Press, New York, pp. 122–130.

Burchfiel, B.C., Molnar, P., Zhao, Z., K'uangyi, L., Wang, S., Huang, M., and Sutter, J., 1989, Geology of the Ulugh Muztagh area, northern Tibet: Earth Planet. Sci. Lett., v. 94, pp. 57–70, http://dx.doi.org/10.1016/0012-821X(89)90083-6.

Bureau Geological and Mineral Resources (BGMR) Qinghai Province, 1991i. Regional Geology of Qinghai Province. Geological Publishing House, Beijing (in Chinese).

Carslaw, H.S., Jaeger, C.J., 1959. Conduction of Heat in Solids. third ed. Clarendon Press, Oxford, p. 510.

Cassata, W.S., Renne, P.R., 2013. Systematic variations of argon diffusion in feldspars and implications for thermochronometry. Geochim. Cosmochim. Acta 112, 251–287. http://dx.doi.org/10.1016/j.gca.2013.02.030.

Champagnac, J.-D., Molnar, P., Anderson, R.S., Sue, C., Delacou, B., 2007. Quaternary erosion-induced isostatic rebound in the western Alps. Geology 35, 195–198.

Chen, W.-P., Chen, C.-Y., Nabelek, J.L., 1998. Present-day deformation of the Qaidam basin with implications for intra-continental tectonics. Tectonophysics 305, 165–181.

Clark, M.K., Farley, K.A., Zheng, D., Wang, Z., Duvall, A.R., 2010. Early Cenozoic faulting of the northern Tibetan Plateau margin from apatite (U–Th)/He ages. Earth Planet. Sci. Lett. 296, 78–88.

Cui, J.W., Tang, Z.M., Deng, J.F., Yue, Y.J., Meng, L.S., Yu, Q.F., 1999. Altyn Fault System. Geology Press, Beijing, pp. 52–226.

Dai, J., Wang, C., Hourigan, J., Santosh, M., 2013. Multi-stage tectono-magmatic events of the Eastern Kunlun Range, northern Tibet: insights from U–Pb geochronology and (U–Th)/He thermochronology. Tectonophysics 599, 97–106.

Ding, Q.F., Jiang, S.Y., Sun, F.Y., 2014. Zircon U–Pb geochronology, geochemical and Sr–Nd–Hf isotopic compositions of the Triassic granite and diorite dikes from the Wulonggou mining area in the Eastern Kunlun Orogen, NW China: petrogenesis and tectonic implications. Lithos 205, 266–283.

Dupont-Nivet, G., Krijgsman, W., Langereis, C.G., Abels, H.A., Dai, S., Fang, X., 2007. Tibetan plateau aridification linked to global cooling at the Eocene–Oligocene transition. Nature 445, 635–638.

Ehlers, T.A., 2005. Crustal thermal processes and the interpretation of thermochronometer data. Rev. Mineral. Geochem. 58, 315–350.

Ehlers, T.A., Farley, K.A., 2003. Apatite (U–Th)/He thermochronometry: methods and applications to problems in tectonic and surface processes. Earth Planet. Sci. Lett. 206, 1–4.

Evans, N.J., Byrne, J.P., Keegan, J.T., Dotter, L.E., 2005a. Determination of Uranium and Thorium in zircon, apatite, and fluorite: application to laser (U–Th)/He thermochronology. J. Anal. Chem. 60 (12), 1159–1165.

Evans, N.J., Wilson, N.S.F., Cline, J.S., McInnes, B.I.A., Byrne, J., 2005b. Fluorite (U–Th)/He thermochronology: constraints on the low temperature history of Yucca Mountain, Nevada. Appl. Geochem. 20, 1099–1105.

Farley, K.A., 2000. Helium diffusion from apatite: general behavior as illustrated by Durango fluorapatite. J. Geophys. Res. 105, 2903–2914.

Farley, K.A., 2002. (U–Th)/He Dating: Techniques, Calibrations, And Applications. In: Porcelli, P.D., Ballentine, C.J., Wieler, R. (Eds.), Noble Gas Geochemistry. Reviews in Mineralogy and Geochemistry Vol. 47, pp. 819–843.

Farley, K.A., Wolf, R.A., Silver, L.T., 1996. The effects of long alpha-stopping distances on (U–Th)/He ages. Geochim. Cosmochim. Acta 60, 4223–4229.

Fu, B., Awata, Y., 2007. Displacement and timing of left-lateral faulting in the Kunlun fault zone, northern Tibet, inferred from geologic and geomorphic features. J. Asian Earth Sci. 29, 253–265. http://dx.doi.org/10.1016/j.jseaes.2006.03.004.

Gautheron, C., Tassan-Got, L., 2010. A Monte Carlo approach to diffusion applied to noble gas/helium thermochronology. Chem. Geol. 273 (3–4), 212–224.

Graham, S.A., Chamberlain, C.P., Yue, Y., Ritts, B.D., Hanson, A.D., Horton, T.W., Waldbauer, J.R., Poage, M.A., Feng, X., 2005. Stable isotope records of Cenozoic climate and topography, Tibetan plateau and Tarim basin. Am. J. Sci. 305, 101–118.

Guan, P., Jian, X., 2013. The Cenozoic sedimentary record in Qaidam Basin and its implications for tectonic evolution of the Northern Tibetan plateau. Acta Sedimentol. Sin. 31, 824–833.

Harris, N.B.W., Ronghua, X., Lewis, C.L., Hawkesworth, C.J., Yuquan, Z., 1988. Isotope Geochemistry of the 1985 Tibet Geotraverse, Lhasa to Golmud. Philos. Trans. R. Soc. Lond. A 327, 263–285.

Herman, F., Braun, J., Dunlap, W.J., 2007. Tectonomorphic scenarios in the Southern Alps of New Zealand. J. Geophys. Res. 112, B04201. http://dx.doi.org/10.1029/2004JB003472.

Huang, H., Niu, Y.L., Nowell, G., Zhao, Z.D., Yu, X.H., Zhu, D.C., Mo, X.X., Ding, S., 2014. Geochemical constraints on the petrogenesis of granitoids in the East Kunlun orogenic belt, northern Tibetan plateau: implications for continental crust growth through syn-collisional felsic magmatism. Chem. Geol. 370, 1–18.

Jolivet, M., Brunel, M., Seward, D., Xu, Z., Yang, J., Malavieille, J., Roger, F., Leyreloup, A., Arnaud, N., and Wu, C., 2003, Neogene extension and volcanism in the Kunlun fault zone, northern Tibet: new constraints on the age of the Kunlun fault. Tectonics, v. 22, p. 1052, http://dx.doi.org/10.1029/2002TC001428.

Ketcham, R.A., Donelick, D.A., Carlson, W.D., 1999. Variability of apatite fission-track annealing kinetics: III. Extrapolation to geologic time scales. Am. Mineral. 84, 1235–1255.

Lease, R.O., Burbank, D.W., Gehrels, G.E., Wang, Z., Yuan, D., 2007. Signatures of mountain building: detrital zircon U/Pb ages from northeastern Tibet. Geology 35 (3), 239–242.

Lee, J.K.W., 1995. Multipath diffusion in geochronology. Contrib. Mineral. Petrol. 120, 60–82. http://dx.doi.org/10.1007/BF00311008.

Li, R., Pei, X., Li, Z., Sun, Y., Pei, L., Chen, G., Chen, Y., Liu, C., Wei, F., 2013. Regional tectonic transformation in East Kunlun Orogenic Belt in early Paleozoic: constraints from the geochronology and geochemistry of Heleganqnaren alkali-feldspar granite. Acta Geol. Sin. 87, 333–345.

Liu, Y., Genser, J., Neubauer, F., Jin, W., Ge, X., Handler, R., Takasu, A., 2005. 40Ar/39Ar mineral ages from basement rocks in the Eastern Kunlun Mountains, NW China, and their tectonic implications. Tectonophysics 398, 199–224.

Lovera, O.M., Richter, F.M., Harrison, T.M., 1989. The 40Ar/39Ar thermochronology for slowly cooled samples having a distribution of diffusion domain sizes. J. Geophys. Res. 94, 17917–17935. http://dx.doi.org/10.1029/JB094iB12p17917.

Lovera, O.M., Richter, F.M., Harrison, T.M., 1991. Diffusion domains determined by 39Ar released during step heating. J. Geophys. Res. 96, 2057–2069. http://dx.doi.org/10.1029/90JB02217.

Lovera, O.M., Grove, M., Harrison, T.M., Mahon, K.I., 1997. Systematic analysis of K-feldspar 40Ar/39Ar step heating results I: significance of activation energy determinations. Geochim. Cosmochim. Acta 61, 3171–3192. http://dx.doi.org/10.1016/S0016-7037(97)00147-6.

Lovera, O.M., Grove, M., Harrison, T.M., 2002. Systematic analysis of K-feldspar 40Ar/39Ar step heating results II: relevance of laboratory argon diffusion properties to nature. Geochim. Cosmochim. Acta 66, 237–1255. http://dx.doi.org/10.1016/S0016-7037(01)00846-8.

Matte, P., Tapponnier, P., Arnaud, N., Bourjot, L., Avouac, J.P., Vidal, P., Liu, Q., Pan, Y., Wang, Y., 1996. Tectonics of Western Tibet, between the Tarim and Indus. Earth and Planet. Sci. Lett. 14, 311–330.

McDowell, F.W., McIntosh, W.C., Farley, K.A., 2005. A precise 40Ar–39Ar reference age for the Durango apatite (U–Th)/He and fission-track dating standard. Chem. Geol. 214, 249–263.

Meng, Q.-R., Fang, X., 2008. Cenozoic tectonic development of the Qaidam Basin in the northeastern Tibetan plateau. In: Burchfiel, B.C., Wang, E. (Eds.), Investigations into the Tectonics of the Tibetan Plateau: Geological Society of America Special Paper 444, pp. 1–24. http://dx.doi.org/10.1130/2008.2444(01).

Me'tivier, F., 1996. Volumes se'dimentaires et bilans de masse en Asie pendant le Ce'nozo¨que PhD Thesis University of Paris, VII, p. 255.

Mock, C., Arnaud, N., and Cantagrel, J.-M., 1999, An early unroofing in Northeastern Tibet? Constraints from 40Ar/39Ar thermochronology on granitoids from the eastern Kunlun range (Qinghai, NW China): Earth Planet. Sci. Lett., v. 171, p. 107–122, http://dx.doi.org/10.1016/S0012-821X(99)00133-8.

Molnar, P., 2004. Late Cenozoic increase in accumulation rates of terrestrial sediment: how might climate change have affected erosion rates? Annu. Rev. Earth Planet. Sci. 32, 67–89.

Molnar, P., England, P., 1990. Late Cenozoic uplift of mountain ranges and global climate change: chicken or egg? Nature 346, 29–34.

Molnar, P., Stock, J.M., 2009. Slowing of India's convergence with Eurasia since20Ma andits implications for Tibetan mantle dynamics. Tectonics 28. http://dx.doi.org/10.1029/2008TC002271.

Montgomery, D.R., 1994. Valley incision and the uplift of mountain peaks. J. Geophys. Res. 99, 13913–13921.

Moore, M.A., England, P.C., 2001. On the inference of denudation rates from cooling ages of minerals. Earth Planet. Sci. Lett. 185, 265–284.

Parsons, I., Gerald, J.D.F., Heizler, M.T., Heizler, L.L., Ivanic, T., Lee, M.R., 2013. Eight-phase alkali feldspars: low-temperature cryptoperthite, peristerite and multiple replacement reactions in the Klokken intrusion. Contrib. Mineral. Petrol. 165, 931–960. http://dx.doi.org/10.1007/s00410-012-0842-5.

Qiu, N., 2002. Thermal evaluation and hydrocarbon generation history of the sedimentary basins in Western China. Pet. Explor. Dev. 29, 6–8.

Reiners, P.W., Nicolescu, S., 2006. Measurement of parent nuclides for (U–Th)/He chronometry by solution sector ICP-MS. ARHDL Report 1 (http://www.geo.arizona.edu/~reiners/arhdl/arhdl.htm).

Rowley, D.B., 1996. Age of initiation of collision between India and Asia: a review of stratigraphic data. Earth Planet. Sci. Lett. 145, 1–13.

Sambridge, M., 1999a. Geophysical inversion with a neighbourhood algorithm — I. Searching a parameter space. Geophys. J. Int. 138, 479–494.

Sambridge, M., 1999b. Geophysical inversion with a neighbourhood algorithm — II. Appraising the ensemble. Geophys. J. Int. 138, 727–746.

Small, E., Anderson, R.S., 1998. Pleistocene relief production in Laramide mountain ranges, western Unites States. Geology 26, 123–126.

Sun, J., Ni, X., Bi, S., Wu, W., Ye, J., Meng, J., Windley, B.F., 2014. Synchronous turnover of flora, fauna, and climate at the Eocene–Oligocene boundary in Asia. Sci. Rep. 4, 7463. http://dx.doi.org/10.1038/srep07463.

Tapponnier, P., Xu, Z., Roger, F., Meyer, B., Arnaud, N., Wittlinger, G., Yang, J., 2001. Oblique stepwise rise and growth of the Tibet plateau. Science 294, 1671–1677. http://dx.doi.org/10.1126/science.105978.

Valla, P.G., Herman, F., van der Beek, P.A., Braun, J., 2010. Inversion of thermochronological age–elevation profiles to extract independent estimates of denudation and relief history — I: theory and conceptual model. Earth Planet. Sci. Lett. 295, 511–522.

van der Beek, P.A., Valla, P.G., Herman, F., Braun, J., Persano, C., Dobson, K.J., Labrin, E., 2010. Inversion of thermochronological age–elevation profiles to extract independent estimates of denudation and relief history — II: application to the French Western Alps. Earth Planet. Sci. Lett. 296, 9–22.

Van der Woerd, J., Ryerson, F.J., Tapponnier, P., Gaudemer, Y., Finkel, R.C., Meriaux, A.S., Caffee, M.W., Zhao, G., He, Q., 1998. Holocene leftlateral slip-rate determined by cosmogenic surface dating on the Xidatan segment of the Kunlun fault (Qinghai, China). Geology 26, 695–698. http://dx.doi.org/10.1130/0091-7613(1998)026<0695:HLSRDB>2.3.CO;2.

Vermeesch, P., 2010. Helioplot, and the treatment of overdispersed (U–Th–Sm)/He data. Chem. Geol. 271, 108–111.

Wang, E., Burchfiel, B.C., 2004. Late Cenozoic right-lateral movement along the Wenquan fault and associated deformation: implications for the kinematic history of the Qaidambasin, Northeastern Tibetan Plateau. Int. Geol. Rev. 46 (10), 861–879.

Wang, X., Wang, B., Qiu, Z., Xie, G., Xie, J., Downs, W., Qiu, Z., Deng, T., 2003. Danghe area (western Gansu, China) biostratigraphy and implications for depositional history and tectonics of northern Tibetan Plateau. Earth Planet. Sci. Lett. 208, 253–269.

Wang, F., Lo, C., Li, Q., Yeh, M., Wan, J., Zheng, D., and Wang, E., 2004Onset timing of significant unroofing around Qaidam Basin, northern Tibet, China: constraints from 40Ar/39Ar and FT thermochronology on granitoids: J. Asian Earth Sci., v. 24, p. 59–69, http://dx.doi.org/10.1016/j.jseaes.2003.07.004.

Wang, F., Lu, X., Lo, C.-H., Wu, F.Y., Yang, L., Zhu, R.X., 2007. Post-collisional, potassic monzonite-minette complex (Shahewan) in the qinling mountains (central China): 40Ar/39Ar thermochronology, petrogenesis, and implications for the dynamic setting of the Qinling orogen. J. Asian Earth Sci. 31, 153–166. http://dx.doi.org/10.1016/j.jseaes.2007.06.002.

Wang, C., Zhao, X., Liu, Z., Lippert, P.C., Graham, S.A., Coe, R.S., Yi, H., Zhu, L., Liu, S., Li, Y., 2008. Constraints on the early uplift history of the Tibetan Plateau. Proc. Natl. Acad. Sci. U. S. A. 105, 4987–4992.

Wang, F., Zheng, X.S., Lee, I.K., Choe, W.H., Evans, N., Zhu, R.X., 2009. An 40Ar/39Ar geochronology on a mid-Eocene igneous event on the Barton and Weaver peninsulas: implication for the dynamic setting of the Antarctic Peninsula. Geochem. Geophys. Geosyst. 10 (12), Q12006. http://dx.doi.org/10.1029/2009GC002874.

Wang, J., Hu, X., Jansa, L., Huang, Z., 2011. Provenance of the Upper Cretaceous–Eocene deep-water sandstones in Sangdanlin, southern Tibet: constraints on the timing of initial India–Asia collision. J. Geol. 119, 293–309. http://dx.doi.org/10.1086/659145.

Wang, F., Wang, Q.C., Lin, W., Wu, L., Shi, W., Feng, H., Zhu, R.X., 2014. 40Ar/39Ar geochronology of the North China and Yangtze cratons: new constraints on Mesozoic cooling and cratonic destruction under East Asia. J. Geophys. Res. 119, 3700–3721. http://dx.doi.org/10.1002/2013JB010708.

Wolf, R.A., Farley, K.A., Silver, L.T., 1996. Helium diffusion and low temperature thermochronometry of apatite. Geochim. Cosmochim. Acta 60, 4231–4240.

Xiong, F.H., Ma, C.Q., Jiang, H.A., Liu, B., Huang, J., 2014a. Geochronology and geochemistry of Middle Devonian mafic dykes in the East Kunlun orogenic belt, Northern Tibet Plateau: implications for the transition from Prototethys to Paleotethys orogeny. Chemie Erde – Geochem. 74, 225–235.

Yan, M.D., Van der Voo, R., Fang, X.M., Pares, J.M., Rea, D.K., 2006. Paleomagnetic evidence for a mid-Miocene clockwise rotation of about 25 degrees of the Guide Basin area in NE Tibet. Earth Planet. Sci. Lett. 241, 234–247.

Yang, J., Xu, Z., Li, H., Shi, R., 2005. The paleo-Tethyan volcanism and plate tectonic regime in the A'nyemaqen region of East Kunlun, northern Tibet Plateau. Acta Petrol. Mineral. 24, 369–380.

Yin, A., Dang, Y., Zhang, M., McRivette, M.W., Burgess, W.P., Chen, X., 2007. Cenozoic Tectonic Evolution of Qaidam Basin and its Surrounding Regions (Part 2): Wedge Tectonics in Southern Qaidam Basin and the Eastern Kunlun Range. In: Sears, J.W., Harms, T.A., Evenchick, C.A. (Eds.), Whence the Mountains? Inquiries into the Evolution of Orogenic Systems: A Volume in Honor of Raymond A: Geol. Soc, Am. Spec http://dx.doi.org/10.1130/2007.2433.

Yin, A., Dang, Y., Wang, L., Jiang, W., Chen, X., Gehrels, G.E., McRivette, M.W., 2008. Cenozoic tectonic evolution of Qaidam basin and its surrounding regions (part 1): the southern Qilian Shan-Nan Shan thrust belt and northern Qaidam basin. Geol. Soc. Am. Bull. 120, 813–846.

Yuan, W., Dong, J., Wang, S., Carter, A., 2006. Apatite fission track evidence for Neogene uplift in the eastern Kunlun Mountains, northern Qinghai–Tibet Plateau, China. J. Asian Earth Sci. 27, 847–856.

Zeitler, P.K., Meltzer, A.S., Koons, P.O., Craw, D., Hallet, B., Chamberlain, C.P., Kidd, W.S.F., Park, S.K., Seeber, L., Bishop, M., Shroder, J., 2001. Erosion, Himalayan geodynamics, and the geomorphology of metamorphism. GSA Today 11, 4–9.

Zhang, P., Molnar, P., Downs, W.R., 2001. Increased sedimentation rates and grain sizes 2–4 myr ago due to the influence of climate change on erosion rates. Nature 410, 891–897.

Zhang, Y.F., Pei, X.Z., Ding, S.P., Li, R.B., Feng, J.Y., Sun, Y., Li, Z.C., Chen, Y.X., 2010. LA-ICPMS zircon U–Pb age of quartz diorite at the Kekesha area of Dulan County, eastern section of the East Kunlun orogenic belt, China and its significance. Geol. Bull. China 29, 79–85.

Zhang, J., Ma, C., Xiong, F., Liu, B., Li, J., Pan, Y., 2014. Early Paleozoic high-Mg diorite-granodiorite in the eastern Kunlun Orogen, western China: response to continental collision and slab break-off. Lithos 210–211, 129–146.